Inorganic Chemistry

Article

pubs.acs.org/IC

Crystal Growth, Structure, Polarization, and Magnetic Properties of Cesium Vanadate, $Cs_2V_3O_8$: A Structure–Property Study

Jeongho Yeon,[†] Athena S. Sefat,[‡] T. Thao Tran,[§] P. Shiv Halasyamani,[§] and Hans-Conrad zur Loye*[,†]

[†]Department of Chemistry and Biochemistry, University of South Carolina, Columbia, South Carolina 29208, United States

[‡]Materials Science and Technology Division, Oak Ridge National Laboratory, Oak Ridge, Tennessee 37831, United States

[§]Department of Chemistry, University of Houston, Houston, Texas 77204, United States

Supporting Information

ABSTRACT: Cesium vanadate, $Cs_2V_3O_8$, a member of the fresnoite-type structure, was synthesized via a hydrothermal route and structurally characterized by single-crystal X-ray diffraction. $Cs_2V_3O_8$ crystallizes in a noncentrosymmetric polar space group, *P4bm*, with crystal data of a = 8.9448(4) Å, c = 6.0032(3) Å, V = 480.31(4) Å^3, and Z = 2. The material exhibits a two-dimensional layered crystal structure consisting of corner-shared $V^{5+}O_4$ and $V^{4+}O_5$ polyhedra. The layers are separated by the cesium cations. The alignment of the individual polyhedra results in a macroscopic polarity for $Cs_2V_3O_8$. Frequency-dependent polarization measurements indicate that the material is not ferroelectric. A pyroelectric coefficient of −2.0 μC m^{-2} K^{-1} was obtained from pyroelectric measurements taken as a function of the temperature. The magnetic susceptibility data were measured as a function of the temperature and yielded an effective magnetic moment of 1.78 μ_B for the V^{4+} cation. Short-range magnetic ordering was observed around 7 K. The susceptibility data were fit to the Heisenberg square-lattice model supporting that the short-range magnetic interactions are antiferromagnetic and two-dimensional. IR and thermal properties were also characterized.

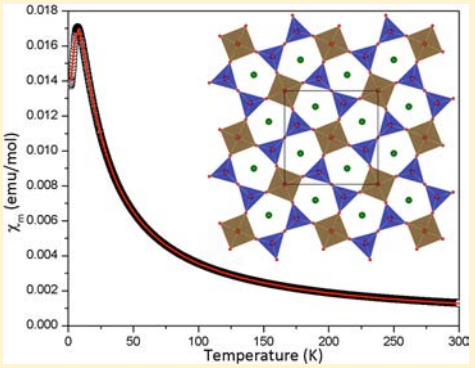

INTRODUCTION

Vanadium oxides continue to attract considerable attention because of their ability to act as catalysts,[1−3] as cathode materials in batteries,[4−6] as intercalation hosts,[7−9] as ion-exchange materials,[10,11] and as magnetic materials[12−15] and for their structural versatility.[16−22] These diverse attributes originate from the various coordination environments and oxidation states found for vanadium in complex oxides. In vanadates, vanadium is typically observed in a tetrahedral, a square-planar, or an octahedral coordination environment and is found in oxidation states of 3+, 4+, or 5+. Exotic magnetic properties sometimes arise from the presence of the V^{4+} cation in a structure;[23−27] however, such tetravalent vanadates are quite rare compared to trivalent and pentavalent vanadates. To investigate the relationship between the structure of V^{4+}-containing oxides and their properties, we set out to synthesize reduced vanadates, specifically oxides containing V^{4+}, to investigate their structures and magnetic properties.

Among complex oxides containing the magnetic V^{4+} ion, the fresnoite-type vanadates have been the most intensively studied oxides because of their low-dimensional magnetic properties.[28−30] The fresnoite-type structure has the general formula $A_2MM'_2O_8$ (A = Sr^{2+} or Ba^{2+}, M = Ti^{4+}, and M′ = Si^{4+} or Ge^{4+}), which consists of a two-dimensional layered-type crystal structure.[31−33] It is known that the tetravalent metal cations in this structure (Ti^{4+}, Si^{4+}, or Ge^{4+}) can be substituted for by either V^{4+} or V^{5+} cations because of their very similar ionic sizes.[34] Typically, charge balance is maintained by the simultaneous substitution of two alkali metals for the A cations, resulting in a structural family with composition $A_2V_3O_8$ (A = K, Rb, Cs, or NH_4). Several investigations of the magnetism and structure of this series of complex oxides concluded that the $A_2V_3O_8$ series exhibits antiferromagnetic coupling and undergoes a structural phase transition as a function of the temperature.[28,35,36] Detailed experimental and theoretical investigations of $K_2V_3O_8$ suggest that it is best thought of as a spin $^1/_2$ quasi-two-dimensional antiferromagnet.[37−41] In this series, structural phase transitions were observed for $K_2V_3O_8$ and $Rb_2V_3O_8$ at 110 and 270 K, respectively, and as a function of the pressure for $(NH_4)_2V_3O_8$.[35,36,42,43] To date, all published investigations reported describe the potassium-, rubidium-, and ammonium-containing members of this series and not, however, the cesium-containing compound. This motivated us to investigate the synthesis and investigation of the properties of the reduced cesium vanadate, $Cs_2V_3O_8$.

Several synthetic routes have been reported for the synthesis of the $A_2V_3O_8$ (A = K, Rb, and NH_4) series, including flux reactions to grow single crystals and conventional solid-state routes to prepare polycrystalline powders.[34−36,41] All of the reported syntheses were carried out at temperatures in excess of 500 °C. Our initial attempts to prepare $Cs_2V_3O_8$ by modifying

Received: March 11, 2013
Published: May 9, 2013

   dx.doi.org/10.1021/ic400601n | *Inorg. Chem.* 2013, 52, 6179−6186

the known synthetic routes were unsuccessful because of, as it turned out, the thermal instability of $Cs_2V_3O_8$ above 500 °C. We therefore developed a new synthetic route based on a low-temperature, two-step hydrothermal approach, where we used oxalic acid to create and stabilize V^{4+} in solution prior to initiating the crystallization of $Cs_2V_3O_8$.

The crystal structure of $Cs_2V_3O_8$ belongs to the fresnoite-type structure and adopts the parent *P4bm* framework. Structures crystallizing in the *P4bm* space group are polar and, thus, are of general interest for their potential NLO, ferroelectric, pyroelectric, or multiferroic behavior.[44−48] These phenomena are associated with the acentricity and polarity of the crystal structure, consisting of local asymmetric units. The alignment of the individual asymmetric units (polyhedra) in the same direction generates a macroscopic polarity in the crystal structure. The material reported herein, $Cs_2V_3O_8$, is polar because of the alignment of the VO_4 and VO_5 polyhedra in the structure, which enabled us to measure its polarization properties.

In this paper, we report on the synthesis, structural characterization, polarization and magnetic property measurement, and overall structure−property relationships of $Cs_2V_3O_8$, which is a new member of the $A_2V_3O_8$ (A = K, Rb, or NH_4) family of reduced vanadates.

EXPERIMENTAL SECTION

Reagents. Cs_2CO_3 (Alfa Aesar, 99.9%), V_2O_5 (Alfa Aesar, 99.6%), and $H_2C_2O_4{\cdot}2H_2O$ (Alfa Aesar, 98%) were used as received.

Synthesis. Single crystals of the reported material were grown via a two-step hydrothermal synthesis. A mixture containing 1 mmol of V_2O_5, 1.5 mmol of $H_2C_2O_4{\cdot}2H_2O$, and 1 mL of H_2O was placed inside a 23 mL Teflon-lined autoclave. The autoclave was closed, heated to 150 °C at a rate of 5 °C min^{-1}, held for 12 h, and cooled to room temperature at a rate of 3 °C min^{-1}. The autoclave was opened, and 2 mmol of Cs_2CO_3 was added to the product from the first reaction, dark-brown solids suspended in a blue solution. The hydrothermal reaction was repeated, however, using reaction times and cooling rates of 24 h and 0.1 °C min^{-1}, respectively. Once cold, the mother liquor was decanted and the solid product was isolated by vacuum filtration and washed with distilled water and acetone. The product consisted of deep-brown single crystals of $Cs_2V_3O_8$ along with unidentified impurities that were removed by sonication. The yield was approximately 91% based on V_2O_5. The powder X-ray diffraction (PXRD) pattern collected on ground crystals indicates that no impurities are contained in the final isolated product.

Single-Crystal X-ray Diffraction. X-ray diffraction intensity data from a plate crystal were measured at room temperature on a Bruker SMART APEX diffractometer (Mo Kα radiation, λ = 0.71073 Å). The raw area detector data frames were processed with *SAINT+*.[49] An absorption correction based on the redundancy of equivalent reflections was applied to the data with *SADABS*.[49] The reported unit cell parameters were determined by least-squares refinement of a large array of reflections taken from each data set. Difference Fourier calculations and full-matrix least-squares refinement against F^2 were performed with *SHELXTL*.[50]

$Cs_2V_3O_8$ crystallizes in the noncentrosymmetric space group *P4bm*, as determined by the successful solution and refinement of the structure. The asymmetric unit contains one cesium, two vanadium, and four oxygen atoms. The cesium atom, one vanadium atom [V(2)], and one oxygen atom [O(3)] are located on a mirror plane (Wyckoff site 4c). The other vanadium atom [V(1)] and one oxygen atom [O(1)] reside on a 4-fold axis (Wyckoff site 2a). The two residual oxygen atoms [O(2) and O(4)] lie on a general position (Wyckoff site 8d) and a 2-fold axis combined with mirror planes (Wyckoff site 2b), respectively. All atoms were refined with anisotropic displacement parameters. Crystallographic data, atomic positions, and selected interatomic distances are listed in Tables 1−3, respectively.

Table 1. Crystallographic Data for $Cs_2V_3O_8$

formula	$Cs_2V_3O_8$
fw	546.64
cryst syst	tetragonal
space group	*P4bm* (No. 100)
a (Å)	8.9448(4)
c (Å)	6.0032(3)
V (Å^3)	480.31(4)
Z	2
density (Mg/m^3)	3.780
abs coeff (mm^{-1})	10.335
cryst size (mm^3)	0.10 × 0.06 × 0.02
θ range	3.22−28.27
reflns collected	5917
indep reflns	645 (R_{int} = 0.0331)
completeness to θ_{max} (%)	100
R_{int}	0.0331
GOF (F^2)	1.433
$R(F)^a$	0.0256
$R_w(F_o^2)^b$	0.0615
extinction coeff	0.0089(6)
Flack parameter	0.00(8)
residual electron density (e Å^{-3})	0.652 and −1.471

$^aR(F) = \sum||F_o| - |F_c||/\sum|F_o|$. $^bR_w(F_o^2) = [\sum w(F_o^2 - F_c^2)^2/\sum w(F_o^2)^2]^{1/2}$.

Table 2. Selected Interatomic Distances (Å) for $Cs_2V_3O_8$

Cs(1)−O(2)	3.152(5)	V(1)−O(1)	1.614(12)
Cs(1)−O(2)	3.152(5)	V(1)−O(2)	1.982(5)
Cs(1)−O(2)	3.431(5)	V(1)−O(2)	1.982(5)
Cs(1)−O(2)	3.431(5)	V(1)−O(2)	1.982(5)
Cs(1)−O(3)	2.966(8)	V(1)−O(2)	1.982(5)
Cs(1)−O(3)	3.103(6)	V(2)−O(2)	1.704(5)
Cs(1)−O(3)	3.103(6)	V(2)−O(2)	1.704(5)
Cs(1)−O(4)	3.080(7)	V(2)−O(3)	1.632(8)
Cs(1)−O(2)	3.152(5)	V(2)−O(4)	1.806(4)
Cs(1)−O(2)	3.152(5)		

Table 3. Atomic Coordinates and Equivalent Isotropic Displacement Parameters (Å^2) for $Cs_2V_3O_8$

	x	y	z	$U_{eq}{}^a$
Cs(1)	0.1710(1)	0.3290(1)	0.7174(1)	0.027(1)
V(1)	0	0	0.1886(4)	0.013(1)
V(2)	0.1330(1)	0.6331(1)	0.1914(3)	0.012(1)
O(1)	0	0	0.4574(19)	0.027(2)
O(2)	0.0844(5)	0.8053(5)	0.0938(9)	0.018(1)
O(3)	0.1279(6)	0.6279(6)	0.4631(14)	0.027(2)
O(4)	0	0.5	0.0824(15)	0.018(2)

$^aU_{eq}$ is defined as one-third of the trace of the orthogonalized U_{ij} tensor.

Powder X-ray Diffraction (PXRD). PXRD data were collected on a Rigaku D/Max-2100 powder X-ray diffractometer using Cu Kα radiation. The step-scan covered the angular range 10−70° 2θ in steps of 0.04°. No impurities were observed, and the calculated and experimental PXRD patterns are in excellent agreement (see Figure S1 in the Supporting Information, SI).

IR Spectroscopy. IR spectra were recorded on a PerkinElmer, Spectrum 100, FT-IR spectrometer in the 650−1100 cm^{-1} range.

Thermal Analyses. Thermogravimetric analysis (TGA) was carried out on a TA Instruments SDT Q600 by heating the sample at a rate of 10 °C min^{-1} under flowing N_2 gas up to a temperature of

dx.doi.org/10.1021/ic400601n | Inorg. Chem. 2013, 52, 6179−6186

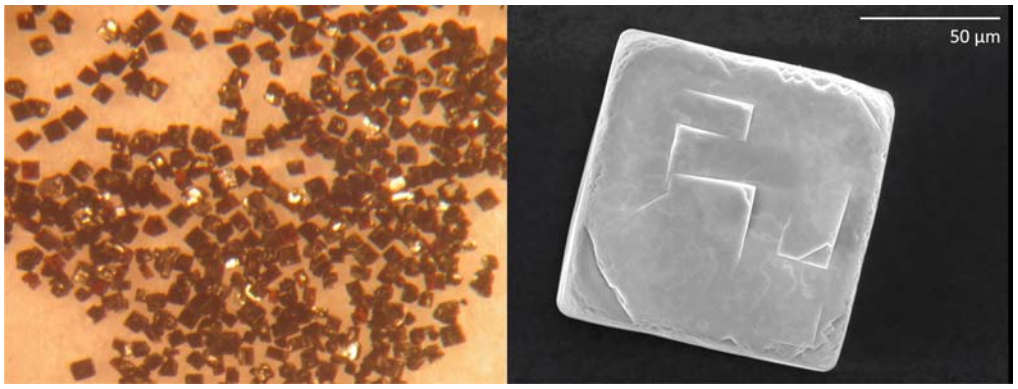

Figure 1. Optical (left) and SEM (right) images of single crystals of $Cs_2V_3O_8$.

550 °C. Differential scanning calorimetry (DSC) was also carried out on a TA Instruments DSC Q2000 by heating the sample at a rate of 10 °C min^{-1} from −50 and +550 °C and cooling it back down to room temperature.

Scanning Electron Microscopy (SEM). A scanning electron micrograph of a single crystal of $Cs_2V_3O_8$ was obtained using a Tescan Vega-3 SEM instrument utilized in the low-vacuum mode. A SEM image of a representative single crystal of $Cs_2V_3O_8$ is shown in Figure 1. Energy-dispersive spectroscopy (EDS) using a Thermo EDS detector equipped on a Tescan instrument also verified the presence of cesium, vanadium, and oxygen in $Cs_2V_3O_8$.

Second-Harmonic Generation (SHG). Powder SHG measurements were performed on a modified Kurtz nonlinear-optical (NLO) system using a pulsed Nd:YAG laser with a wavelength of 1064 nm. Comparisons with known SHG materials were made using ground crystalline α-SiO_2. A detailed description of the equipment and methodology has been published elsewhere.[44,51] No index-matching fluid was used in any of the experiments.

Piezoelectric Measurements. Converse piezoelectric measurements were performed using a Radiant Technologies RT66A piezoelectric test system with a TREK high-voltage amplifier, a Precision Materials Analyzer, a Precision High Voltage Interface, and an MTI 2000 Fotonic Sensor. The $Cs_2V_3O_8$ sample was pressed into a pellet (∼1.3 cm diameter and ∼1 mm thickness) and sintered at 350 °C for 7 days. Silver paste was applied to both sides of the pellet, and the pellet was cured at 300 °C for 12 h. The same pellet was also used for polarization measurements.

Polarization Measurements. The polarization was measured on a Radiant Technologies RT66A ferroelectric test system with a TREK high-voltage amplifier between 70 and 180 °C in a Delta 9023 environmental test chamber. The unclamped pyroelectric coefficient, defined as dP/dT (change in the polarization with respect to a change in the temperature), was determined by measuring the polarization as a function of the temperature. A detailed description of the methodology used has been published elsewhere.[44] To measure any possible ferroelectric behavior, the polarization was measured at room temperature under a static electric field of 9 kV cm^{-1} with frequencies of 100−1000 Hz. For the pyroelectric measurements, the polarization was measured statically from 70 to 180 °C in 10 °C increments, maintaining an electric field of 7 kV cm^{-1} throughout the measurement. The temperature was allowed to stabilize before the polarization was measured.

Magnetic Measurements. The direct-current (dc) magnetization was measured as a function of the temperature using a Quantum Design MPMS SQUID magnetometer or an EverCool Dewar magnetometer system. The polycrystalline samples were placed in a gelatin capsule, secured by a small amount of epoxy. In a typical temperature sweep experiment, the sample was cooled to 2 K under zero-field-cooled (zfc) conditions and data were collected by heating the sample from 2 to 300 K in an applied field of 1000 Oe. The sample was then cooled in the applied field (field-cooled, fc) to 2 K, while data were collected.

RESULTS AND DISCUSSION

Synthesis. The synthesis of reduced vanadates requires an approach that allows for the formation and stabilization of V^{4+}. The $A_2V_3O_8$ (A = K, Rb, and NH_4) family was reportedly synthesized via either solid-state routes or electrochemical reduction.[34,36,38,52,53] Specifically, to prepare polycrystalline samples, ternary precursors of AVO_3 were reacted with appropriate amounts of V_2O_3 or V_2O_5, whereas single crystals were grown out of KVO_3 or $Rb_2V_4O_9$/RbBr fluxes or via reduction of V_2O_5 using RbI as a reducing agent. We attempted all of the above methods to prepare $Cs_2V_3O_8$; however, all attempts were unsuccessful, apparently because of the high stability of $CsVO_3$,[54] CsV_2O_5,[55] and $Cs_2V_4O_9$[56] that formed preferentially. We were unable to detect any amount of $Cs_2V_3O_8$ in the reaction products, which consisted of mixtures of vanadates, including $CsVO_3$, CsV_2O_5, and $Cs_2V_4O_9$. We attempted a hydrothermal route using V_2O_5, Cs_2CO_3, and oxalic acid as our starting materials. The desired mixed-valent vanadium, 4+/5+, could be expected because oxalic acid is known to be a mild reducing agent. In addition, we were able to carry out hydrothermal synthesis at much lower temperatures (∼150 °C) than the reported solid-state synthetic conditions (∼550 °C). Unfortunately, although many permutations of the experimental conditions were pursued, the simultaneous reaction of Cs_2CO_3, V_2O_5, and oxalic acid always resulted in a mixture of an unidentified phase (major product), $CsVO_3$ (major product), and $Cs_2V_3O_8$ (minor product). To obtain a single-phase product of $Cs_2V_3O_8$, we had to modify the hydrothermal route and separate it into two sequential steps: (1) reduction of the vanadium precursor and (2) reaction of the reduced vanadium species with cesium. This two-step hydrothermal route, as described in detail in the Experimental Section, resulted in high-quality crystals of $Cs_2V_3O_8$ in high yield, as shown in Figure 1. The PXRD pattern collected on ground crystals is in excellent agreement with the diffraction pattern calculated using the single-crystal data (see Figure S1 in the SI). To test the generality of this two-step hydrothermal route, we also synthesized two other known members of this family, namely, $K_2V_3O_8$ and $Rb_2V_3O_8$. Here, also, the two-step process worked with remarkable success and resulted in the synthesis of pure crystals of $K_2V_3O_8$ and $Rb_2V_3O_8$. The PXRD patterns of these two compounds collected on ground crystals are also in excellent agreement with the calculated powder patterns (see Figure S2 in the SI).

Structure. The title compound, $Cs_2V_3O_8$, crystallizes in the noncentrosymmetric polar space group *P4bm* and exhibits a two-dimensional crystal structure consisting of sheets of corner-

dx.doi.org/10.1021/ic400601n | *Inorg. Chem.* 2013, 52, 6179−6186

shared VO_4 and VO_5 polyhedra. As shown in Figure 2, the corner-sharing VO_5 polyhedra are isolated from each other by

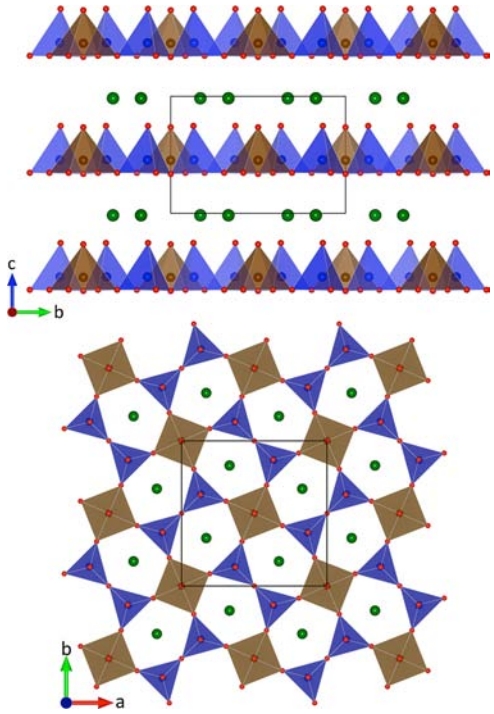

Figure 2. Polyhedral structure representation of $Cs_2V_3O_8$ along the (top) *a* and (bottom) *c* axes. The two-dimensional layers consist of corner-shared VO_5 and VO_4 polyhedra; only five-membered rings are observed in the layer. The brown, blue, green, and red spheres/polyhedra represent V^{4+}, V^{5+}, K^+, and O^{2-} ions, respectively.

V_2O_7 groups, resulting in $V_3O_8^{2-}$ layers in the *ab* plane, which is characteristic for the fresnoite-type structure. The $V_3O_8^{2-}$ layers, which stack in the *c* direction, are separated by two Cs^+ cations. One interesting structural feature is the presence of five-membered rings, composed of two VO_5 and three VO_4 polyhedra, in the layer, with the Cs^+ cations located at the approximate center of the rings and approximately midway between the layers. This arrangement aligns the layers and places them exactly above and below each other, forming an infinite, aligned stack. The V^{4+} cation is found only in the VO_5 square pyramids, with V−O bond distances ranging from 1.614(12) to 1.982(5) Å, while the V^{5+} cation is located only in the VO_4 tetrahedra with V−O bond distances of 1.632(8)−1.806(4) Å. The Cs^+ cations are coordinated to 10 oxygen atoms, 5 located in the layer above and 5 located in the layer below, with the Cs−O distances ranging from 2.966(8) to 3.665(5) Å. Bond Valence Sum (BVS) calculations[57,58] resulted in values of 3.93, 5.19, and 1.18 for V^{4+}, V^{5+}, and Cs^+, respectively, and are consistent with the expected values, confirming the presence of the V^{4+} in the structure.

Figure 3 shows the interlayer separation distances for the $A_2V_3O_8$ (A = K, Rb, Cs, and NH_4) series. It is expected that the interlayer distance will increase with the increasing sizes of the cation located between the $V_3O_8^{2-}$ sheets and that this would be reflected in the length of the *c* axis. Hence, the interlayer distance for $Cs_2V_3O_8$ should be the greatest because the ionic radius of Cs^+ is the largest within this series. As seen in Figure 3, the length of the *c* axis increases in the order of the K, Rb, NH_4, and Cs cation sizes, consistent with the expected trend. On the other hand, the ratio of a'/c ($a' = a/\sqrt{2}$; see Figure 4) decreases for the same sequence. If the a'/c ratio reaches a value of 1, then the vanadium positions in the structure can be described using a primitive cubic sublattice. $Cs_2V_3O_8$, with an a'/c ratio of 1.05, approaches this ratio and, thus, has a pseudocubic sublattice for the vanadium cations. The observed trend of the a'/c ratio as a function of the cation size for this series indicates that the presence of a larger cation between the layers not only forces the layers further apart along the *c* axis but also expands the sheet uniformly in the *ab* plane, resulting in a smaller a'/c ratio.

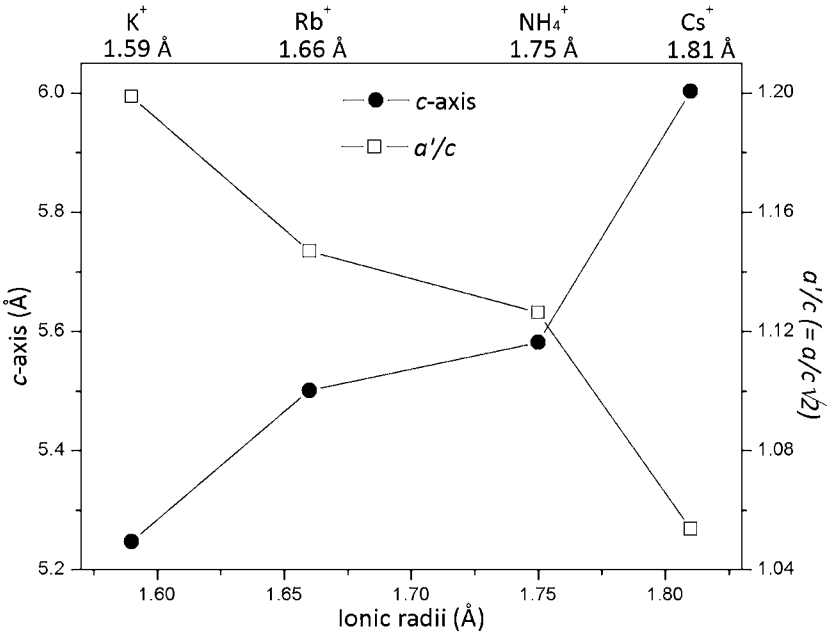

Figure 3. Plot of the A cation size versus the length of the *c* axis and the ratio of a'/c ($a' = a/\sqrt{2}$) for the $A_2V_3O_8$ (A = K, Rb, NH_4, and Cs) series. The circles and squares are for the K, Rb, NH_4, and Cs phases from left to right.

dx.doi.org/10.1021/ic400601n | *Inorg. Chem.* 2013, 52, 6179−6186

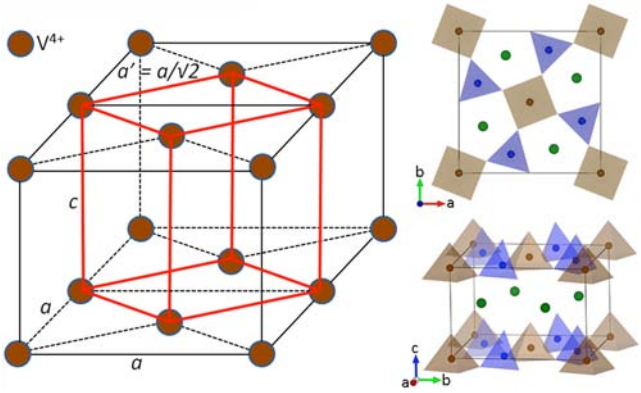

Figure 4. Doubled unit cell toward the *a* axis containing only V^{4+} cations (left), where the red solid lines represent a new primitive lattice. Note that when $a' = c$ ($a' = a/\sqrt{2}$), the primitive cell becomes a cubic lattice. The unit cell of $Cs_2V_3O_8$ is shown on the right, where the brown, blue, and green spheres/polyhedra represent V^{4+}, V^{5+}, and K^+ ions, respectively. For clarity, oxygen atoms are omitted.

The crystal structure of $Cs_2V_3O_8$ and the $A_2V_3O_8$ (A = K, Rb, Cs, and NH_4) family in general are closely related to that of the polar $A_3V_5O_{14}$ (A = K, Rb, and Tl) series (see Figure 5).[59] Both

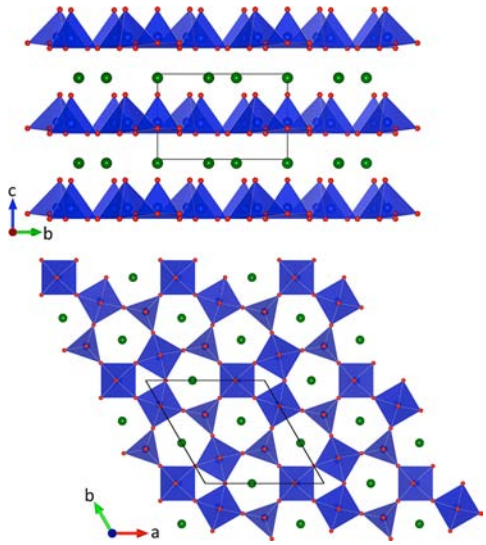

Figure 5. Polyhedral structure representation of $A_3V_5O_{14}$ (A = K, Rb, and Tl) along the (top) *a* and (bottom) *c* axes. The two-dimensional layers consist of corner-shared VO_5 and VO_4 polyhedra; both three- and five-membered rings are found in the layer. The blue, green, and red spheres/polyhedra represent V^{5+}, K^+, and O^{2-} ions, respectively.

structural families exhibit a similar two-dimensional layered crystal structure consisting of corner-shared VO_4 and VO_5 polyhedra, where the layers are separated by the A^+ cations. However, while the $A_2V_3O_8$ family contains the magnetic cation V^{4+} (d^1), in the square-pyramidal sites, the $A_3V_5O_{14}$ family contains only V^{5+} (d^0) cations. The origin for this difference lies in the fact that V_2O_7 groups isolate the VO_5 square pyramids in the $A_2V_3O_8$ structure, while V_3O_{12} groups isolate the VO_4 tetrahedra in the $A_3V_5O_{14}$ structure. As a result, only five-membered rings are observed in $A_2V_3O_8$, while three- and five-membered rings are found in $A_3V_5O_{14}$. Although detailed arrangements of the polyhedra in the sheet structures differ slightly between these two families, in both families the polyhedra that are aligned in the same direction in each layer to create the permanent polarity throughout the crystal structures.

In order to better understand the origin of the polarity, local dipole moments of the individual polyhedra were examined.[60,61] For any materials to be considered polar, they must crystallize in 1 of 10 crystal classes (1, 2, 3, 4, 6, *m*, *mm*2, 3*m*, 4*mm*, and 6*mm*), and a polar direction can be defined as one of crystal axes.[62] When asymmetric units exhibit a local dipole moment and when the individual polyhedra align in the same direction, then a macroscopic polarity can be created, which determines the magnitude of several functional properties. The space group of the title compound, *P*4*bm*, belongs to the 4*mm* crystal class, indicating that $Cs_2V_3O_8$ is polar. As seen in Figure 2 and Table 2, the VO_4 and VO_5 polyhedra exhibit one short and three and four, respectively, longer bonds, where the short axial bonds are oriented parallel to the *c* axis. Thus, a net dipole moment from the individual polyhedra is observed along the *c* axis, which can be defined as the polar axis for $Cs_2V_3O_8$. The calculated dipole moments, 1.13 and 0.30 for the VO_5 and VO_4 polyhedra, respectively, are relatively small compared to values found in highly asymmetric coordination environments created by lone-pair cations. This suggests that the measured polarization of $Cs_2V_3O_8$ will be fairly small, consistent with the polarization measurements discussed below.

IR Spectroscopy. The IR spectrum for the reported material was collected between 650 and 1100 cm^{-1}. The bands observed above 750 cm^{-1} can be attributed to V−O vibrational modes, whereas the V−O−V vibrational modes appear below 750 cm^{-1}. These assignments are consistent with previously reported data.[63] The IR spectrum is given in Figure S3 in the SI.

Thermal Analyses. The thermal behavior of $Cs_2V_3O_8$ was investigated using TGA and DSC. As seen in Figure S4 in the SI, no weight loss is observed up to 550 °C under a N_2 flow; however, the structure decomposes near 500 °C. Using PXRD, the residues of decomposition were identified as $CsVO_3$,[54] CsV_2O_5,[56] and at least one other unidentified phase.

It is known that $K_2V_3O_8$ and RbV_3O_8, two members of the $A_2V_3O_8$ (A = K, Rb, Cs, and NH_4) family, undergo a structural phase transition from *P*4*bm* to *P*4$_2$*bc* or *P*4*nc* for $K_2V_3O_8$ and to *P*4*bm*(00γ) superspace group symmetry for $Rb_2V_3O_8$, respectively, at low temperature.[35,36] To determine if $Cs_2V_3O_8$ also undergoes a low-temperature phase transition, DSC measurement was performed between −50 and +550 °C. During the heating cycle, the DSC data contain an endothermic peak at about 500 °C, corresponding to decomposition of $Cs_2V_3O_8$, while exothermic peaks, observed during the cooling cycle, are most likely due to crystallization of the decomposition products. PXRD measurements demonstrated that the residues were the same as those found in the TGA experiment. Thus, both TGA and DSC measurements shed light on why $Cs_2V_3O_8$ could not be synthesized by us via a solid-state route. It appears that $Cs_2V_3O_8$ is unstable at temperatures above 500 °C and decomposes into CsV_2O_5, $CsVO_3$, and at least one other phase. Hence, our two-step hydrothermal route provides a convenient method to prepare $Cs_2V_3O_8$ at low temperatures, thereby avoiding its instability at higher temperatures.

No evidence for a structural phase transition was observed in the DSC data, suggesting that either none exists or it takes place at a temperature lower than −50 °C. A unit cell collected on a single crystal at 100 K gave a *P*4*bm* unit cell with lattice parameters of a = 8.947(1) Å and c = 5.945(1) Å, values that are almost identical with the ones collected at room

dx.doi.org/10.1021/ic400601n | Inorg. Chem. 2013, 52, 6179−6186

temperature. We therefore conclude that there is no structural phase transition as a function of the temperature down to 100 K.

SHG and Piezoelectric Properties. All materials that crystallize in one of the noncentrosymmetric crystal classes, except 432, may exhibit SHG and piezoelectric behavior. Although $Cs_2V_3O_8$ belongs to this class, none of these properties were observed in $Cs_2V_3O_8$, most likely because the magnitude of its dipole moment is very small. Large SHG efficiency and strong piezoelectric responses are typically correlated with large dipole moments.[64−66] Because the dipole moment in $Cs_2V_3O_8$ is very small, any SHG or piezoelectric response that might exist was below the detection limit of the measurements.

Polarization Properties. Although the local dipole moment of $Cs_2V_3O_8$ is small, its polar space group, *P*4*bm*, indicates that it exhibits a macroscopic polarity arising from the alignment of the individual polyhedra in the sheets, which indicates the possibility of observing ferroelectric or pyroelectric behavior in $Cs_2V_3O_8$. In order for a material to exhibit ferroelectric behavior, the macroscopic polarity must be reversed under an external applied electric field. The polarization measurement has to be performed at several frequencies because ferroelectric behavior is strongly frequency-dependent. The observed polarization loops from the frequency-dependent measurements, as shown in Figure 6, are not ferroelectric

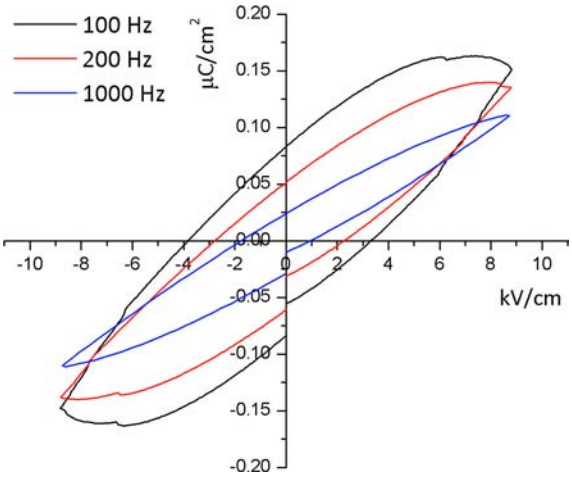

Figure 6. Frequency-dependent polarization measurements for $Cs_2V_3O_8$. The measured polarization loops are not ferroelectric hysteresis loops but rather are due to dielectric loss.

hysteresis loops, however, but rather are likely due to dielectric loss.[67] In other words, the observed macroscopic polarity cannot be reversed under an external electric field. To better understand this lack of polarization reversal, it is important to examine the local coordination environment of the VO_4 and VO_5 polyhedra because macroscopic polarization reversal results from the reversal of polarization of the individual polyhedra. As mentioned earlier, the macroscopic polarity stems from the alignment of these individual polyhedra, where the contribution of the VO_4 polyhedra is much less because of its tetrahedral coordination environment. Any polarization reversal thus has to result from the VO_5 polyhedra. In the well-known ferroelectric materials of $BaTiO_3$ and $KNbO_3$, the polarization reversal involves the physical displacement of octahedrally coordinated metal cations, i.e., Ti^{4+} and Nb^{5+}.[68] One way for the dipole moment to be reversed in $Cs_2V_3O_8$ would involve the displacement of the vanadium cation along the *c* axis, i.e., toward or away from the basal plane of the VO_5 square pyramid. This displacement is, however, energetically unfavorable because the shifted vanadium cation loses coordination with the axial oxide ligand of the square pyramid, which essentially prevents ferroelectric behavior.

Although $Cs_2V_3O_8$ is not ferroelectric, the polar space group still implies that the material may exhibit pyroelectric behavior. Pyroelectricity is formally defined as the temperature dependence of the spontaneous polarization with a pyroelectric coefficient, $p = (\partial Ps/\partial T)$, where Ps is the spontaneous polarization and T is the temperature. The pyroelectric coefficient (p), the change in polarization as a function of the temperature, was determined with a value of $-2.0\ \mu C\ m^{-2}\ K^{-1}$, which is consistent with other nonferroelectric pyroelectric materials (see Figures S5 and S6 in the SI).[45]

Magnetic Properties. The temperature dependence of the magnetic and inverse susceptibilities for $Cs_2V_3O_8$ in an applied field of 1000 Oe is shown in Figure 7. In the high-temperature range of 100−300 K, the inverse susceptibility data were fit to the modified Curie−Weiss law with a temperature-independent paramagnetic term (χ_{TIP}), $\chi = C/(T - \theta) + \chi_{TIP}$, which resulted in values of 0.392 emu K mol^{-1}, −10.4 K, and 1.73×10^{-5} emu mol^{-1} for the Curie constant, the Weiss temperature, and χ_{TIP}, respectively. From the Curie constant, the effective magnetic moment of 1.77 μ_B per V^{4+} was calculated, which is in good agreement with the expected spin-only value of 1.73 μ_B per V^{4+}, confirming the existence of the V^{4+} magnetic ion in $Cs_2V_3O_8$. The magnetization increases with decreasing temperature, and a relatively broad maximum is observed at around 7 K, suggesting the presence of short-range antiferromagnetic interactions. As shown in Figure 8, the $\chi_m T$ data plotted as a function of the temperature decreases gradually as the temperature decreases, indicating the presence of antiferromagnetic interactions, which is consistent with the negative Weiss constant from the Curie−Weiss fit.

In order to model the short-range magnetic correlations, several low-dimensional magnetic exchange models could be considered, including dimer, one-dimensional infinite-chain, and two-dimensional square-lattice models. The dimer model can be readily excluded because no dimeric magnetic exchange pathways are found in the crystal structure. The only possible way for a one-dimensional chain model to be applied to the structure of $Cs_2V_3O_8$ would require the magnetic exchange interactions to proceed via the axial oxygen atoms between the layers; however no isolated magnetic pathways exist within the layers because of the equivalent V^{4+}−V^{4+} distances. These exchange interactions, however, involve extremely long separations (4.390 Å) between the V^{4+} cations and the axial oxygen atoms in adjacent layers, suggesting that this model is not likely to apply to $Cs_2V_3O_8$.

On the basis of the crystal structure, the two-dimensional square-lattice model appears to be the most appropriate model for $Cs_2V_3O_8$, which includes the magnetic interaction pathways of V^{4+}−O−O−V^{4+} or V^{4+}−O−V^{5+}−O−V^{4+}. To better examine this model, the two-dimensional Heisenberg model[34,69] (eq 1) was utilized to fit the susceptibility data.

$$\chi_m = \frac{N\mu_B{}^2 g^2}{|J|}\left[3x + \sum_{n=1}^{6}\frac{C_n}{x^{n-1}}\right]^{-1} + \frac{C}{T-\theta} + \chi_{TIP} \quad (1)$$

dx.doi.org/10.1021/ic400601n | Inorg. Chem. 2013, 52, 6179−6186

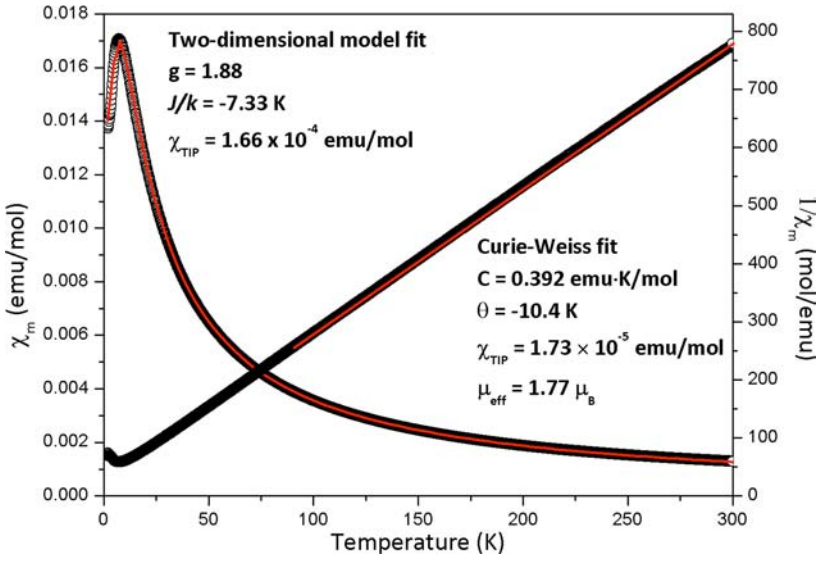

Figure 7. Temperature dependence of the molar magnetic susceptibility (left axis) and of the inverse susceptibility, χ_m^{-1} (right axis), of $Cs_2V_3O_8$, measured in an applied field of 1000 Oe. The red solid lines represent the fit based on a combined two-dimensional square lattice and Curie–Weiss law model.

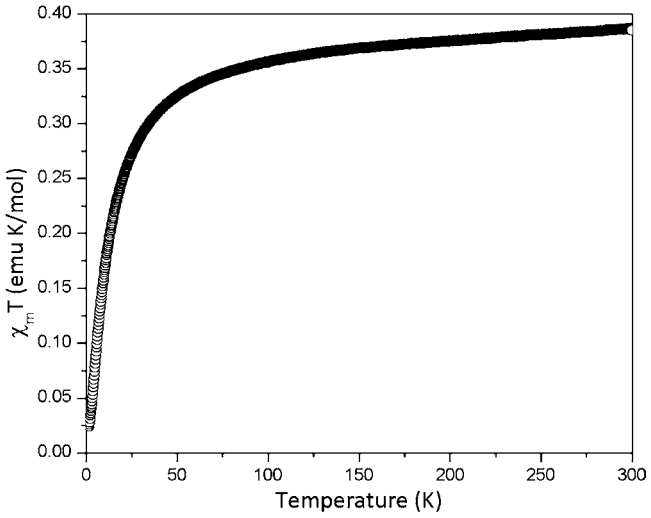

Figure 8. Plot of $\chi_m T$ vs Temperature (K) for $Cs_2V_3O_8$. Data were collected in an applied field of 1000 Oe.

Equation 1: $x = kT/JS(S + 1)$, N is Avogadro's number, μ_B is the Bohr magneton, g is the Lande g factor, J is the magnetic exchange parameter, T is the temperature, and C_n are coefficients calculated by lines.

As shown in Figure 7, a good fit of the susceptibility data could be obtained using the two-dimensional Heisenberg model. The fit gave values of 1.88, −7.33 K, and 1.66×10^{-4} emu mol^{-1} for the g factor, J/k, and χ_{TIP}, respectively. These values are in good agreement with data published for application of the two-dimensional Heisenberg model to the magnetic susceptibility data of the previously reported $A_2V_3O_8$ (A = K, Rb, and NH_4) family.[34] It might also be possible to consider three-dimensional interactions, instead of the two-dimensional interactions, because half of the diagonal length of the *ab* plane in the unit cell to the length of the *c* axis is close to 1, as seen in Figure 4, which indicates the possibility of a cubic magnetic sublattice. This model, however, includes the extremely long magnetic exchange pathways of V^{4+}–O···Cs···O–V^{4+} (over 10 Å), suggesting much weaker magnetic interactions compared to those expected within the layers. It is, thus, reasonable to consider $Cs_2V_3O_8$ as a two-dimensional Heisenberg antiferromagnet.

CONCLUSIONS

We have successfully synthesized and characterized the mixed-valent cesium vanadate $Cs_2V_3O_8$. The material exhibits a two-dimensional layered crystal structure consisting of corner-shared VO_4 and VO_5 polyhedra. The individual polyhedra are all aligned along the *c* direction, creating a macroscopic polarization of the structure. The material was not found to be ferroelectric, however. Magnetic measurements were performed that revealed short-range antiferromagnetic interactions around 7 K. The magnetic susceptibility data were successfully fit to the two-dimensional Heisenberg square-lattice model, supporting the theory that the magnetic interactions dominate within the layers.

ASSOCIATED CONTENT

Supporting Information

X-ray data in CIF format, PXRD patterns, IR and UV–vis spectra, TGA diagrams, pyroelectric polarization loops, and pyroelectric coefficients. This material is available free of charge via the Internet at http://pubs.acs.org.

AUTHOR INFORMATION

Corresponding Author

*E-mail: zurloye@mailbox.sc.edu.

Notes

The authors declare no competing financial interest.

ACKNOWLEDGMENTS

Research supported by the U.S. Department of Energy, Office of Basic Energy Sciences, Division of Materials Sciences and Engineering under Award DE-SC0008664. P.S.H. and T.T.T. thank the Welch Foundation for support (Grant E-1457). We thank Dr. Mark D. Smith for the low-temperature unit cell data. We thank Dr. Neil Dilley and Dr. Shi Li at Quantum Design for collecting the magnetic susceptibility data. We also thank Dr.

John E. Greedan for helpful discussions concerning the fit of the magnetic data to the two-dimensional Heisenberg model.

REFERENCES

(1) Taufiq-Yap, Y. H.; Rownaghi, A. A.; Hussein, M. Z.; Irmawati, R. *Catal. Lett.* **2007**, *119*, 64.
(2) Scheurell, K.; Hoppe, E.; Brzezinka, K.-W.; Kemnitz, E. *J. Mater. Chem.* **2004**, *14*, 2560.
(3) Santamaria-Gonzalez, J.; Luque-Zambrana, J.; Merida-Robles, J.; Maireles-Torres, P.; Rodriguez-Castellon, E.; Jimenez-Lopez, A. *Catal. Lett.* **2000**, *68*, 67.
(4) Pralong, V.; Caignaert, V.; Raveau, B. *J. Mater. Chem.* **2011**, *21*, 12188.
(5) Chernova, N. A.; Roppolo, M.; Dillon, A. C.; Whittingham, M. S. *J. Mater. Chem.* **2009**, *19*, 2526.
(6) Whittingham, M. S. *Chem. Rev.* **2004**, *104*, 4271.
(7) Bissessur, R.; MacDonald, J. *Mater. Chem. Phys.* **2007**, *106*, 256.
(8) De, S.; Dey, A.; De, S. K. *J. Phys. Chem. Solids* **2006**, *68*, 66.
(9) De, S.; Dey, A.; De, S. K. *J. Chem. Phys.* **2006**, *125*, 224704/1.
(10) Tengku, A. T. S. M.; Yusoff, A. R. M.; Abdul, K. K. J. *Chromatographia* **2010**, *72*, 141.
(11) Zhang, X.-M.; Tong, M.-L.; Lee, H. K.; Chen, X.-M. *J. Solid State Chem.* **2001**, *160*, 118.
(12) Marino, N.; Lloret, F.; Julve, M.; Doyle, R. P. *Dalton Trans.* **2011**, *40*, 12248.
(13) Djerdj, I.; Cao, M.; Rocquefelte, X.; Cerny, R.; Jaglicic, Z.; Arcon, D.; Potocnik, A.; Gozzo, F.; Niederberger, M. *Chem. Mater.* **2009**, *21*, 3356.
(14) Yan, B.; Maggard, P. A. *Inorg. Chem.* **2007**, *46*, 6640.
(15) Yan, B.; Luo, J.; Dube, P.; Sefat, A. S.; Greedan, J. E.; Maggard, P. A. *Inorg. Chem.* **2006**, *45*, 5109.
(16) Yeon, J.; Kim, S.-H.; Nguyen, S. D.; Lee, H.; Halasyamani, P. S. *Inorg. Chem.* **2012**, *51*, 609.
(17) Dong, B.; Gomez-Garcia, C. J.; Peng, J.; Benmansour, S.; Ma, J. *Polyhedron* **2007**, *26*, 1310.
(18) Jabor, J. K.; Stoesser, R.; Thong, N. H.; Ziemer, B.; Meisel, M. *Angew. Chem., Int. Ed.* **2007**, *46*, 6354.
(19) Xu, Y.; Nie, L.-B.; Zhu, D.; Song, Y.; Zhou, G.-P.; You, W.-S. *Cryst. Growth Des.* **2007**, *7*, 925.
(20) Pitzschke, D.; Jansen, M. *Z. Anorg. Allg. Chem.* **2007**, *633*, 1563.
(21) Dai, Z.; Shi, Z.; Li, G.; Chen, X.; Lu, X.; Xu, Y.; Feng, S. *J. Solid State Chem.* **2003**, *172*, 205.
(22) Millet, P.; Galy, J.; Johnsson, M. *Solid State Sci.* **1999**, *1*, 279.
(23) Yan, Y. J.; Li, Z. Y.; Zhang, T.; Luo, X. G.; Ye, G. J.; Xiang, Z. J.; Cheng, P.; Zou, L. J.; Chen, X. H. *Phys. Rev. B: Condens. Matter Mater. Phys.* **2012**, *85*, 085102/1.
(24) Tsirlin, A. A.; Nath, R.; Abakumov, A. M.; Shpanchenko, R. V.; Geibel, C.; Rosner, H. *Phys. Rev. B: Condens. Matter Mater. Phys.* **2010**, *81*, 174424/1.
(25) Oka, K.; Yamada, I.; Azuma, M.; Takeshita, S.; Satoh, K. H.; Koda, A.; Kadono, R.; Takano, M.; Shimakawa, Y. *Inorg. Chem.* **2008**, *47*, 7355.
(26) Nath, R.; Tsirlin, A. A.; Rosner, H.; Geibel, C. *Phys. Rev. B: Condens. Matter Mater. Phys.* **2008**, *78*, 064422/1.
(27) Tsirlin, A. A.; Belik, A. A.; Shpanchenko, R. V.; Antipov, E. V.; Takayama-Muromachi, E.; Rosner, H. *Phys. Rev. B: Condens. Matter Mater. Phys.* **2008**, *77*, 092402/1.
(28) Rai, R. C.; Cao, J.; Musfeldt, J. L.; Singh, D. J.; Wei, X.; Jin, R.; Zhou, Z. X.; Sales, B. C.; Mandrus, D. *Phys. Rev. B: Condens. Matter Mater. Phys.* **2006**, *73*, 075112/1.
(29) Bogdanov, A. N.; Rossler, U. K.; Wolf, M.; Muller, K. H. *J. Magn. Magn. Mater.* **2004**, *272−276*, 332.
(30) Bogdanov, A. N.; Rossler, U. K.; Wolf, M.; Muller, K. H. *Phys. Rev. B: Condens. Matter Mater. Phys.* **2002**, *66*, 214410/1.
(31) Hoche, T.; Russel, C.; Neumann, W. *Solid State Commun.* **1999**, *110*, 651.
(32) Markgraf, S. A.; Halliyal, A.; Bhalla, A. S.; Newnham, R. E.; Prewitt, C. T. *Ferroelectrics* **1985**, *62*, 17.
(33) Kimura, M.; Doi, K.; Nanamatsu, S.; Kawamura, T. *Appl. Phys. Lett.* **1973**, *23*, 531.
(34) Liu, G.; Greedan, J. E. *J. Solid State Chem.* **1995**, *114*, 499.
(35) Chakoumakos, B. C.; Custelcean, R.; Kamiyama, T.; Oikawa, K.; Sales, B. C.; Lumsden, M. D. *J. Solid State Chem.* **2007**, *180*, 812.
(36) Withers, R. L.; Hoeche, T.; Liu, Y.; Esmaeilzadeh, S.; Keding, R.; Sales, B. *J. Solid State Chem.* **2004**, *177*, 3316.
(37) Choi, K. Y.; Lemmens, P.; Gnezdilov, V. P.; Sales, B. C.; Lumsden, M. D. *Phys. Rev. B: Condens. Matter Mater. Phys.* **2012**, *85*, 144434/1.
(38) Lumsden, M. D.; Nagler, S. E.; Sales, B. C.; Tennant, D. A.; McMorrow, D. F.; Lee, S. H.; Park, S. *Phys. Rev. B: Condens. Matter Mater. Phys.* **2006**, *74*, 214424/1.
(39) Zainullina, V. M.; Volkov, V. L.; Podvalnaya, N. V.; Ivanovskii, A. L. *J. Struct. Chem.* **2005**, *46*, 340.
(40) Sales, B. C.; Lumsden, M. D.; Nagler, S. E.; Mandrus, D.; Jin, R. *Phys. Rev. Lett.* **2002**, *88*, 095901/1.
(41) Lumsden, M. D.; Sales, B. C.; Mandrus, D.; Nagler, S. E.; Thompson, J. R. *Phys. Rev. Lett.* **2000**, *86*, 159.
(42) Grzechnik, A.; Ren, T.-Z.; Posse, J. M.; Friese, K. *Dalton Trans.* **2011**, *40*, 4572.
(43) Choi, J.; Zhu, Z. T.; Musfeldt, J. L.; Ragghianti, G.; Mandrus, D.; Sales, B. C.; Thompson, J. R. *Phys. Rev. B: Condens. Matter Mater. Phys.* **2002**, *65*, 054101/1.
(44) Ok, K. M.; Chi, E. O.; Halasyamani, P. S. *Chem. Soc. Rev.* **2006**, *35*, 710.
(45) Lang, S. B. *Phys. Today* **2005**, *58*, 31.
(46) Lang, S. B.; Das-Gupta, D. K. In *Handbook of Advanced Electronic and Photonic Materials and Devices*; Nalwa, H. S., Ed.; Academic Press: San Francisco, 2001.
(47) Haertling, G. H. *J. Am. Ceram. Soc.* **1999**, *82*, 797.
(48) Auciello, O.; Scott, J. F.; Ramesh, R. *Phys. Today* **1998**, *51*, 22.
(49) *SMART*, version 5.625; *SAINT+*, version 6.45; *SADABS*, version 2.05; Bruker Analytical X-ray Systems, Inc.: Madison, WI, 2001.
(50) *SHELXTL*, version 6.14; Bruker analytical X-ray Systems, Inc.: Madison, WI, 2000.
(51) Kurtz, S. K.; Perry, T. T. *J. Appl. Phys.* **1968**, *39*, 3798.
(52) Ha-Eierdanz, M. L.; Mueller, U. *Z. Anorg. Allg. Chem.* **1992**, *613*, 63.
(53) Andrukaitis, E.; Jacobs, P. W. M.; Lorimer, J. W. *Can. J. Chem.* **1990**, *68*, 1283.
(54) Slobodin, B. V.; Ishchenko, A. V.; Samigullina, R. F.; Teslenko, O. S.; Shul'gin, B. V.; Zhurakovskii, D. Y. *Inorg. Mater.* **2011**, *47*, 1126.
(55) Mumme, W. G.; Watts, J. A. *J. Solid State Chem.* **1971**, *3*, 319.
(56) Liu, G.; Greedan, J. E. *J. Solid State Chem.* **1995**, *115*, 174.
(57) Brese, N. E.; O'Keeffe, M. *Acta Crystallogr.* **1991**, *B47*, 192.
(58) Brown, I. D.; Altermatt, D. *Acta Crystallogr.* **1985**, *B41*, 244.
(59) Yeon, J.; Kim, S.-H.; Halasyamani, P. S. *Inorg. Chem.* **2010**, *49*, 6986.
(60) Debye, P. *Polar Molecules*; Chemical Catalog Co.: New York, 1929.
(61) Debye, P. *Phys. Z.* **1921**, *22*, 302.
(62) Hahn, T. *International Tables for Crystallography, Vol. A, Space Group Symmetry*; Kluwer Academic: Dordrecht, Holland, 2006.
(63) Kristallov, L. V.; Podval'naya, N. V.; Perelyaeva, L. A. *Zh. Neorg. Khim.* **2002**, *47*, 243.
(64) Yeon, J.; Kim, S.-H.; Nguyen, S. D.; Lee, H.; Halasyamani, P. S. *Inorg. Chem.* **2012**, *51*, 2662.
(65) Nguyen, S. D.; Yeon, J.; Kim, S.-H.; Halasyamani, P. S. *J. Am. Chem. Soc.* **2011**, *133*, 12422.
(66) Kim, S.-H.; Yeon, J.; Halasyamani, P. S. *Chem. Mater.* **2009**, *21*, 5335.
(67) Scott, J. F. *J. Phys.: Condens. Matter* **2008**, *20*, 021001/1.
(68) Cohen, R. E. *Nature* **1992**, *358*, 136.
(69) Lines, M. E. *J. Phys. Chem. Solids* **1970**, *31*, 101.